Influence of the microstructure of a Ti5553 titanium alloy on chip morphology and cutting forces during orthogonal cutting

Antoine Pouliquen, Nicolas Chanfreau, Linamaria Gallegos Mayorga, Charles Mareau, Yessine Ayed, Guenael Germain, Moukrane Dehmas

Influence of the microstructure of a Ti5553 titanium alloy on chip morphology and cutting forces during orthogonal cutting

A. Pouliquen [a], N. Chanfreau [b], L. Gallegos-Mayorga [a], C. Mareau [a,*], Y. Ayed [a], G. Germain [a], M. Dehmas [b]

[a] *Arts et Metiers Institute of Technology, LAMPA, HESAM Universite, F-49035 Angers, France*
[b] *CIRIMAT, Université de Toulouse, CNRS, INPT, UPS, 4 allée E. Monso, BP44362, 31030 Toulouse Cedex 04, France*

Keywords:
Titanium alloy
Machining
High-speed imagery
Machine learning
Orthogonal cutting

A B S T R A C T

Titanium alloys, largely used for aeronautical applications, are difficult to machine. High cutting forces, chip serration and important tool wear reflect this poor machinability, limiting productivity. One way of improving the machinability of titanium alloys consists of controlling their microstructure. In the present work, the impact of the microstructure of the Ti5553 alloy on chip formation and cutting forces is investigated. For this purpose, a novel experimental approach is proposed. Orthogonal cutting tests are performed on eight different microstructures, which allows studying the impact of the α-phase fraction as well as the size and shape of α particles. Also, an original post processing method based on machine learning provides chip morphological information from images recorded with two high speed cameras. Such information is completed with the cutting forces measured with a dynamometer. In contrast with commonly used approaches, the proposed method is not limited to the formation of a few segments, but uses the full dataset acquired during a test. The results obtained for the different microstructures indicate that no direct link can be established between the cutting forces and their hardness as minimal cutting forces are obtained for microstructures with an intermediate hardness. For microstructures providing low hardness, high cutting forces result from a significantly thick chip. In opposition, for the microstructures leading to high hardness, an important flow stress generates high cutting forces. This study also suggests that chip morphology is primarily affected by the α-phase fraction while the size and morphology of α-phase particles have little influence.

1. Introduction

Titanium alloys are largely used for aeronautical applications due to their high strength to weight ratio and good resistance to corrosion. However, as a result of their high specific properties and low thermal conductivity, titanium alloys usually display poor machinability in comparison with other metallic alloys (Niknam et al., 2014).

In consequence, different options have been explored to improve their machinability. The first one consists in optimizing processing conditions. As a first lever, the cutting parameters can be adjusted. As shown by Barry et al. (2001) large variations in both cutting forces and chip morphology were found for varying cutting speeds and feed rates for orthogonal cutting. Similarly, Nouari et al. (2008) showed that the tool rake angle along with the feed rate and the cutting speed had an influence on the cutting forces, the chip morphology and the tool wear mechanisms. A second possible lever is assisted machining. For example, Kaynak et al. (2018) investigated the impact of dry, minimum quantity lubrication (MQL), high pressure coolant (HPC) and cryogenic conditions during orthogonal cutting of the Ti5553 alloy. The study showed that HPC improved the breakability of the chip while cryogenic assistance helped reducing cutting temperatures. Both of these techniques also helped to reduce the contact length between the tool and the chip. Moreover, Ayed et al. (2017) highlighted that cryogenic assistance improves tool life and surface integrity. Similar conclusions were drawn by Ayed and Germain (2018) for the use of HPC when machining the Ti5553 alloy. Liu et al. (2022) demonstrated that ultrasonic assistance leads to better surface integrity and enhanced fatigue behaviour when drilling a Ti6Al4V alloy.

As a second option, machinability can also be improved by changing the microstructure of titanium alloys. Indeed, different studies have indicated that machining conditions are impacted by microstructure. For instance, Kieren-Ehses et al. (2021) showed that the chip thickness of a cp-titanium is impacted by crystallographic orientation. According to their results, the effect of crystallographic orientation is reduced when the cutting speed is increased. This local contribution of microstructure

* Corresponding author.
E-mail addresses: antoine.pouliquen@ensam.eu (A. Pouliquen), charles.mareau@ensam.eu (C. Mareau).

https://doi.org/10.1016/j.jmatprotec.2023.118054

Nomenclature

$\bar{a}$	Average value of signal a(t)
φ	Shear angle
a'_p	Actual depth of cut
a_p	Nominal depth of cut
C_a	Cumulative distribution function associated to the energy spectral density of the signal a
$D_{a,b}$	Kolmogorov–Smirnov metric comparing signals a and b
F_z	Cutting force
$f_{90}(a)$	Characteristic frequency of signal a (90%)
l'_c	Actual width of cut
l_c	Nominal width of cut
S_{aa}	Energy spectral density of the signal a
V_c	Cutting speed
cp	Commercially pure
HPC	High Pressure Coolant
MQL	Minimum Quantity Lubrification
SEM	Scanning Electron Microscope
std(a)	Standard deviation of signal a(t)

is complementary with more global studies focusing on the impact of microstructure of titanium alloys during an entire cutting test. For example, Joshi et al. (2014) compared different titanium alloys showing that the shear plane length and the chip segment shape are impacted by the β phase volume fraction. They also found similar responses when comparing the frequency of chip segmentation to variations in cutting forces. Ramirez (2017) observed that chip morphology (segmentation, chip thickness and shear angle) depends on microstructure during orthogonal cutting of the Ti6Al4V alloy. Patil et al. (2016) drew similar conclusions while analysing chip formation during face turning operations. In the context of micro-milling, Attanasio et al. (2013) showed that the microstructure of the Ti6Al4V alloy impacts tool wear and cutting forces. Abbasi et al. (2016) obtained similar results for end-milling operations. For high speed machining, Sharma and Meena (2020) observed that the depth of the deformed zone of the Ti6Al4V alloy depends on the microstructure. Wagner et al. (2019) compared the impact of two different microstructures of the Ti6Al4V alloy on chip formation. The first microstructure was homogeneous and generated mostly regular saw-tooth chips while the second one was heterogeneous and lead to large variations in the shapes of the chip segments. Specifically, the inclination of the lamellae compared to the shear band orientation governed the local chip morphology. The recent study of Suárez Fernández et al. (2021), focused on the Ti6246 alloy, indicated that the cutting force during turning operations is impacted by local variations in microstructure caused by prior forging operations. This study also showed that an increase in α lath thickness is responsible for an increase in machining forces though the hardness decreases.

Imaging techniques are also commonly used to improve the understanding of the process leading to chip formation. In most studies, observations are carried out on a single side of the test specimen and limited to a short period of the cutting operation. For example, Baizeau et al. (2017) used a complementary metal–oxide–semiconductor set in double frame mode to obtain two images with a low interframe time (120 ns) with a resolution of 0.66 µm px^{-1} and an area of observation of 1.7×1.4 mm^2. The recorded images taken before, during and after the cutting process allowed the determination of the kinematic fields during chip formation in the primary shearing zone and machined subsurface. Zhang et al. (2021) used two different systems recording a pair of images with a low interframe time and resolutions of either 0.66 µm px^{-1} or 1.625 µm px^{-1}. The images allowed visualizing the velocity fields near the cutting tool edge. Hijazi and Madhavan (2008) developed an ultra high-speed polyvalent system capable of recording a sequence of eight images or four pairs of stereo images at frame rates up to 10^6 fps to observe chip formation. Using high magnification (0.27 µm px^{-1}) on a small field of view (350 µm × 250 µm) they were able to determine velocity and shear strain rates. These four previous systems focused on the acquisition of images at low interframe time. As a consequence, they did not enable to record the whole process of chip formation. To circumvent this limitation, Pottier et al. (2014) chose a high-speed camera with a frame rate of 18,000 fps and a spatial resolution of 1.65 µm px^{-1} to record a sequence of 2,568 frames with a field of view of 650×600 µm^2. In this study, the post-processing was limited to the formation of a single segment (45 frames). Displacement and strain field analysis allowed the determination of three distinct phases during chip formation. During the first stage, strains are concentrated at the tool tip vicinity before cumulating along the adiabatic shear band during the second one. Finally, strains stabilize while the segment is fully formed. Harzallah et al. (2018) simultaneously recorded IR images and visible images at frame rates and resolutions of respectively 600 fps, 160×120 px^2 and 6,000 fps, 512×512 px^2 (for an observed area of 500×500 µm^2). On a global approach, they studied the evolution of strain and strain rates during chip formation for different cutting speeds. This study showed that both strain rate and strain path depend on the cutting speed.

Since chip formation is a process with strong spatial and temporal localization, an intense light source is needed for image collection. Baizeau et al. (2017) opted for a laser head generating two pulses of 5–8 ns. These sources provide intense light but only for a short period of time, hence they do not enable the analysis of the whole test which lasts around 650 ms. Zhang et al. (2021) indicated that laser-pulsed lighting provided a higher intensity illumination and a better image resolution. In contrast, a LED lighting system, easier to set up, could be used for longer and required less surface preparation. To study the scene for a large period of time, Moulart et al. (2019) used two flashlights of 400 W and a halogen lamp of 500 W. This lighting conditions limited the acquisition rate to 7,000 fps and the cutting speed to 0.6 m s^{-1} in order to obtain the kinematic field at the tool tip. Harzallah et al. (2018) used two high power LEDs (1040 lm) providing diffuse axial illumination for the first one and outside focused light for the second one. The previous detailed studies showed that an intense lighting must be achieved but only for short periods of time to record images at a high frame rate. However, to observe a whole test, a compromise can be found with less powerful lights and lower frame rates.

In the present work, the impact of the microstructure of the Ti5553 alloy on chip morphology and cutting forces during orthogonal cutting is investigated. For this purpose, different heat treatments were selected to control volume fraction, morphology and size of the α-phase particles. The experimental set-up was designed to evaluate cutting forces, shear angle and chip morphology. A novel post-processing procedure that relies on machine learning and spectral analysis is proposed to characterize chip morphology. The obtained results allow discussing the role of microstructure and the connection between cutting forces and chip morphology.

The present paper is organized as follows. The different microstructures, data acquisition and post-treatment procedures are presented in Section 2. The methods used to post-process experimental data are also exposed. The results obtained for the different microstructures are discussed in Section 3. The time-averaged quantities (e.g. cutting force, chip thickness and shear angle) obtained for the different microstructures are compared to one another. The results derived from spectral analysis are finally exposed, which allows discussing the impact of microstructure on the frequency distribution for both the cutting force and the chip thickness.

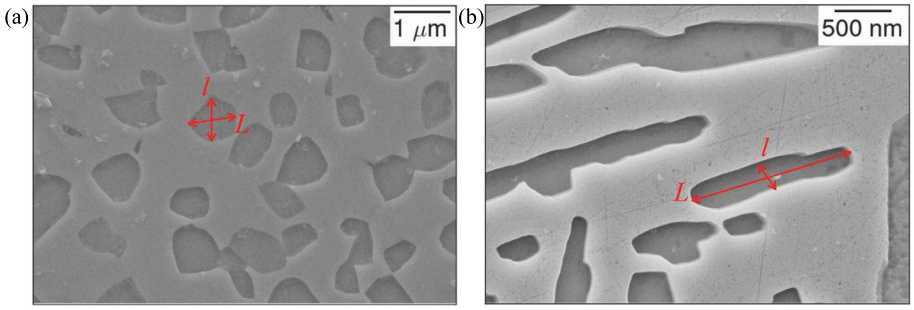

Fig. 1. Method to measure the size of α particles.

2. Experimental methods

2.1. Material and microstructures

The present study focuses on the near-β Ti5553 alloy (Ti-5Al-5V-5Mo-3Cr, wt. %), which displays low machinability in comparison with other titanium alloys. As shown by Arrazola et al. (2009), in comparison with the Ti6Al4V alloy, a higher specific cutting force, a higher specific feed force and a faster tool wear were observed for the Ti5553 alloy. Echoing this previous study, Bouchnak (2010) found higher cutting forces and a higher friction coefficient when comparing these two alloys.

To investigate the influence of microstructure on chip formation and cutting forces, different heat treatments were applied to obtain seven microstructures from the as-received material. After heat treatment, the surface layer was removed to eliminate the possible effect of oxygen diffusion on machining. The metallographic observations, made with a ZEISS SEM, corresponding to the eight different microstructures (seven heat-treated and one as-received) are presented in Fig. 2. Image analysis on at least 20 SEM images and X-ray diffraction analyses were carried out to evaluate the volume fractions, morphologies and sizes of α-phase particles as well as the average β grain size. To determine these quantities, a threshold was applied to metallographic observations to separate α-phase particles from the β-phase matrix. Once this operation was done, the length and width of 200 particles of α phase were measured as shown in Fig. 1. The β grain size was determined thanks to the intercept method introduced by Voort (1999). The results of metallographic observations, which include the mean values and the corresponding standard deviations, are provided in Table 1.

Vickers hardness tests with a load of 1 kg were also performed for each microstructure. The mean values and the corresponding standard deviations, obtained from a minimum of ten measurements, are presented in Table 1.

The microstructures significantly differ from each other with α-phase volume fractions ranging from 0 to 56%. Also, the morphology of α-phase particles is either lamellar (α_{wi}, α_{gb}, α_{wgb}, or α_s) or equiaxed (α_{nod}). The characteristic dimensions of α particles span from 0.1 μm to 12 μm, particles resulting from secondary precipitation (α_s) being much smaller than lamellas formed from grain boundaries (α_{gb} and α_{wgb}). While most microstructures are unimodal, two bimodal microstructures, for which α nodules and secondary α precipitates coexist, are considered (see Table 1). Finally, the average β grain size is about 700 μm for most microstructures. Only the 30 α_{nod}, the 55 bimodal and the 55 as-received microstructures have a lower grain size of 520, 462 and 440 μm respectively.

2.2. Experimental set-up

To investigate the role of microstructure on chip formation and cutting forces, orthogonal cutting tests were performed on the eight microstructures. The corresponding experimental set-up, which was specifically developed for the present study, is shown in Fig. 3. It includes an electrical actuator set to move the specimen towards a fixed cutting tool with a cutting speed V_c of 100 mm s^{-1}. It is worth mentioning that the working length of the actuator (about 370 mm) is higher than the sample length (about 65 mm) so that cutting speed remains constant during the entire cutting test. This cutting speed is typical of the broaching used for some industrial applications (Mo et al., 2005). Uncoated carbide tools provided by SECO Tools AB were used for the orthogonal cutting tests. A new tool was used for each microstructure to limit the impact of tool wear. The inserts had a rake angle of 0°, a clearance angle of 7.5° and a width of 4 mm. After each cutting test, the cutting tool was observed to determine whether the sharpness was affected by prior cutting operations or not. The edge radius of the cutting tool (15 μm±5 μm) is small in comparison with the depth of cut and has small variations. According to the literature (Rech et al., 2004), such variations of the cutting edge radius do not impact significantly the cutting forces. To limit the effect of tool wear, the tool was changed when significant tool wear was detected. A micrometric screw was placed on the tool holder to control the depth of cut a_p, whose nominal value is 250 μm for the present study.

To record the three components (F_x, F_y and F_z) of the cutting force, a Kistler dynamometer 9257B, with an acquisition frequency of 30 kHz, was placed behind the tool holder. It is worth mentioning that, in the present study, the ratio F_x/F_z did not exceed 5%, which confirms that the cutting conditions are representative of orthogonal cutting. In contrast with other experimental studies presented earlier in this paper, the proposed set-up uses two high-speed cameras (Photron NOVA S6) to observe both sides of the specimen. This choice was motivated by post-mortem observations of chips showing important differences regarding chip morphology between both sides. Indeed, because of the ratio between the β grain size and the cut volume, the local microstructure is different for both sides. As a result, since the chip formation process depends on microstructure, the chip morphology is not necessarily identical for both sides. Each camera was equipped with a 12X zoom lens system (NAVITAR) to observe the region near the tool tip. An exposure time of 1/30,000 s and a resolution of 512 × 384 px^2 were used for both cameras. For the seven two-phased microstructures, the spatial resolution was 2.9 μm px^{-1} while the resolution was 3.6 μm px^{-1} for the 100% β microstructure. These resolutions respectively correspond to fields of view of 1.485 × 1.114 mm^2 and 1.818 × 1.363 mm^2. Since the region of interest is small and the acquisition frequency high, an intense light source was included. For the present work, two Blue X-Focus light systems providing an intense light source focused on the tool tip were used. The experimental set-up also included an auxiliary air flow to evacuate any possible smoke resulting from the cutting operation.

The Ti5553 specimens used for the present study were 65 mm long and 40 mm high (Fig. 3 (c)). Their thickness was comprised between 2 mm and 2.5 mm. The lateral faces were polished with silicon carbide grinding papers and diamond paste. Finally, to reveal the underlying microstructure, the entirety of the observed surfaces of the specimens were chemically etched with a corrosive solution ($10H_2SO_4$ + 5HF + $85H_2O$ vol. %) .

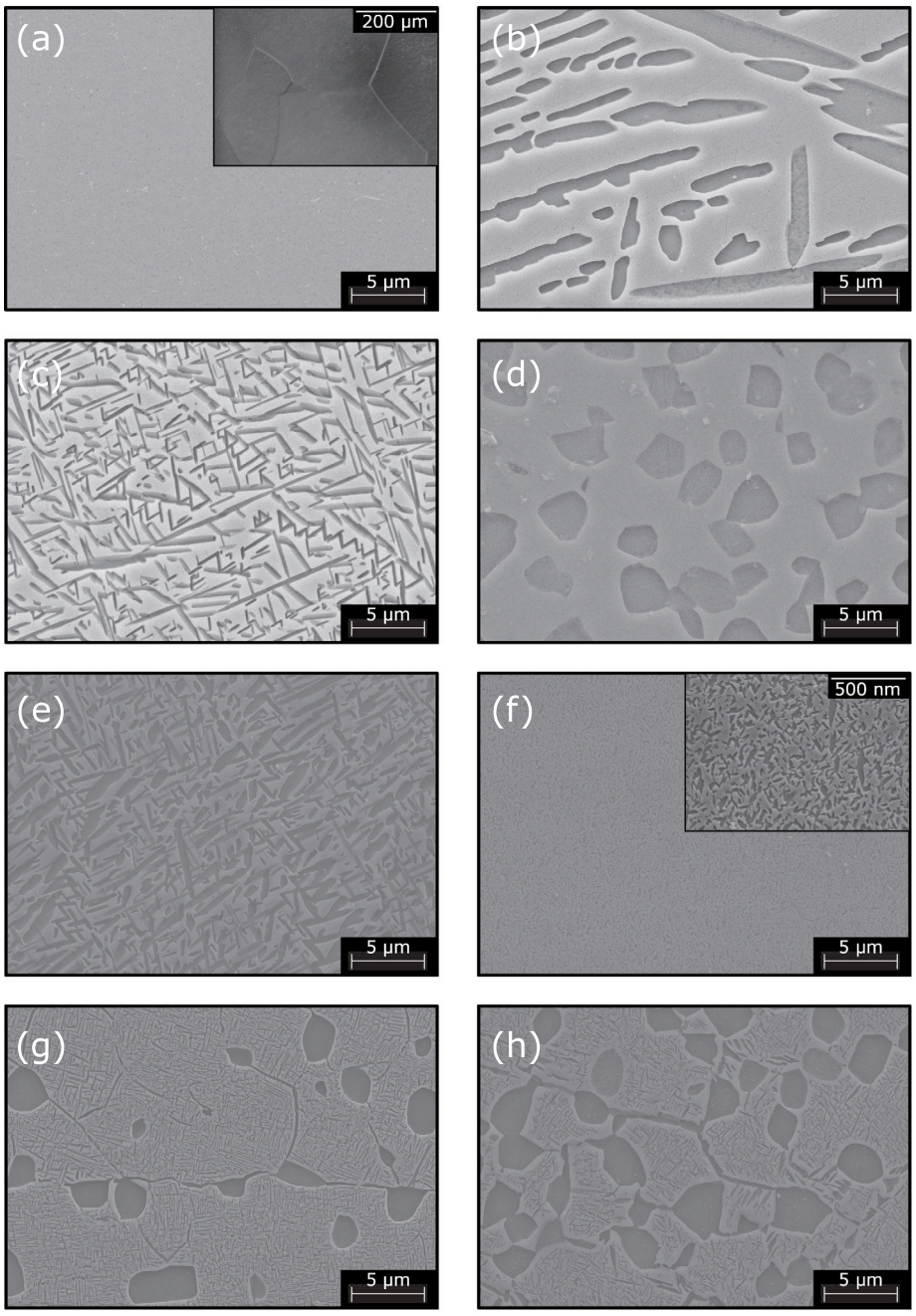

Fig. 2. Metallographic observations of the different microstructures of the Ti5553 alloy: (a) 100 β, (b) 30 α_{gb}, (c) 30 α_{wi}, (d) 30 α_{nod}, (e) 55 α_{wi}, (f) 55 α_{s}, (g) 55 bimodal, (h) 55 as-received with a magnification of x10k.

Cutting tests in two different orthogonal orientations were performed to evaluate an effect of crystallographic texture. Since no pronounced differences in chip formation are observed, the role of the global crystallographic texture on chip formation has not been further investigated.

2.3. Correction of cutting forces

The Kistler dynamometer used to record the cutting forces is based on a piezo-electric technology that may cause the force signal to drift. To compensate the effect of drift, an affine correction was applied to the force signal. The initial (before cutting) and final (after cutting) force values measured by the dynamometer, which should be zero, were used to evaluate the contribution of the drift. This contribution was then subtracted from the original signal to obtain the corrected signal.

When comparing different microstructures, variations in specimen thickness (l_c) and depth of cut (a_p) (Fig. 3 (b)) affecting cutting forces should be taken into account. First, as mentioned in Section 2.1, different specimens do not have the exact same width l_c, whose nominal value is 2.5 mm (varying from 2 mm to 2.5 mm). Second, while the nominal depth of cut a_p is 250 µm, the actual depth of cut, measured from images, is slightly different (from 200 µm to 250 µm). To compare the cutting forces obtained for different microstructures, a normalization procedure was therefore applied to force signals. This procedure assumes that the cutting force depends linearly on the depth of cut and the specimen width. As a result, the normalized cutting force F_z was

Table 1
List of microstructures with the corresponding Vickers hardness (HV1), volume fractions, morphologies and sizes of α-phase particles. When available the mean value of a given measurement is accompanied with ± 1 std of the measured value.

Name	α phase morphology and volume fraction (%vol.)	Average α particle length (μm)	Average α particle width (μm)	Average β grain size (μm)	Hardness (HV1)
100 β	0% α	n/a	n/a	700 ± 36	290 ± 3
30 α_{gb}	33% α_{gb+wgb}	12.3 ± 7.8	1.7 ± 0.5	700	325 ± 5
30 α_{nod}	30% α_{nod}	3.5 ± 1.3	2.4 ± 0.9	520	299 ± 4
30 α_{wi}	34% α_{wi}	1 ± 0.6	0.3 ± 0.1	700	336 ± 3
55 α_{wi}	55% α_{wi}	1.6 ± 0.7	0.4 ± 0.1	700	375 ± 2
55 α_s	55% α_s	0.3 ± 0.1	0.1 ± 0.05	700	432 ± 2
55 bimodal 44% α_s	12% α_{nod} + 2.4 ± 1.1 0.5 ± 0.3	 1.6 ± 0.5 0.1 ± 0.06	462	402 ± 3	
55 as-received	21% α_{nod} + 34% α_s	3.5 ± 1.1 0.7	2.3 ± 0.6 0.2	440	374 ± 1

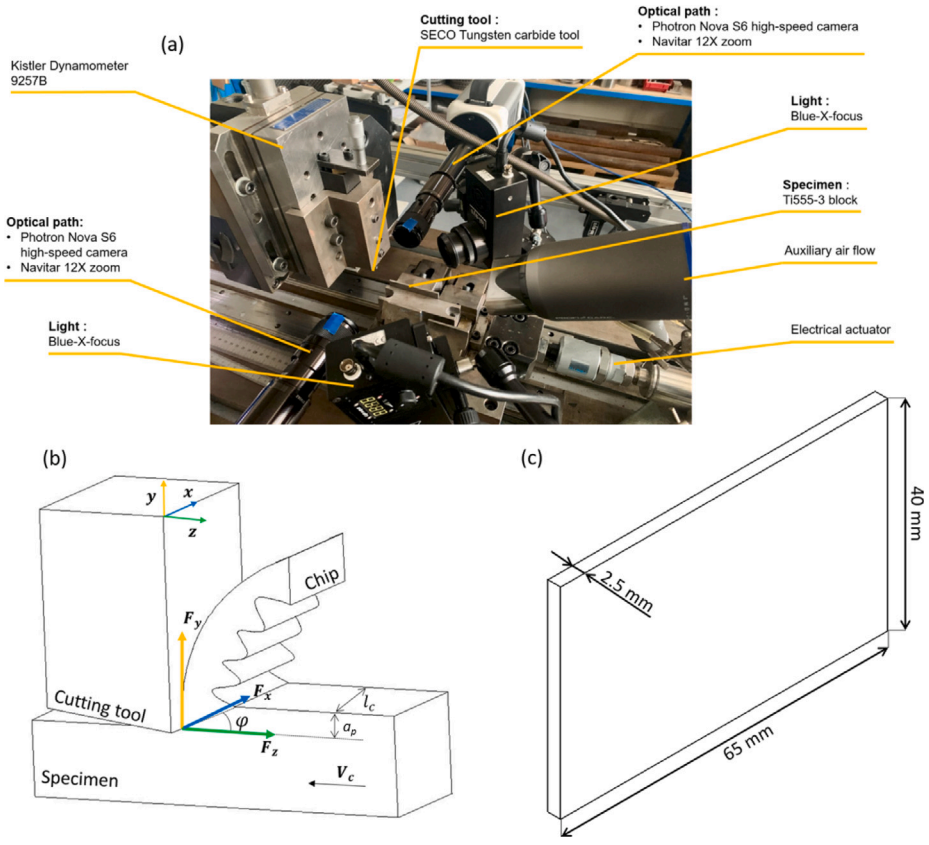

Fig. 3. (a) Experimental set-up, (b) orthogonal cutting principle and (c) specimen geometry.

evaluated from the actual cutting force F_z' with:

$$F_z(t) = F_z'(t) \times \frac{a_p}{a_p'} \times \frac{l_c}{l_c'}, \quad (1)$$

where a_p and l_c (respectively a_p' and l_c') are the nominal (respectively actual) depth of cut and specimen width. It is worth mentioning that cutting forces do not systematically exhibit a linear dependence with respect to the depth and width of cut (Sun et al., 2009). The linear correction procedure however provides satisfactory results in the present study because the variations of the depth and width of cut around their nominal values are limited. Prior to cutting operation, the specimen thickness was measured every 5 mm. A linear interpolation operation was then applied to determine the specific thickness at a given time. The depth of cut was determined at each time t from the images recorded with the high speed cameras. It is worth mentioning that different preliminary cutting tests were carried out to assess the validity of the above relation. By eliminating dimensional effects, this procedure allows considering only microstructural effects when comparing cutting forces.

2.4. Determination of shear angle

For the experimental conditions of the present study, about 20,000 images per camera were obtained for each of the 20 orthogonal cutting tests. An automated procedure is therefore necessary to analyse such an important number of images. A segmentation method relying on machine learning was implemented to perform semantic segmentation on images since they display low contrast, hence not well-suited for a simple threshold operation. Specifically, an U-Net convolutional network derived from (Ronneberger et al., 2015) was used in the present

Fig. 4. Determination of shear angle by image segmentation.

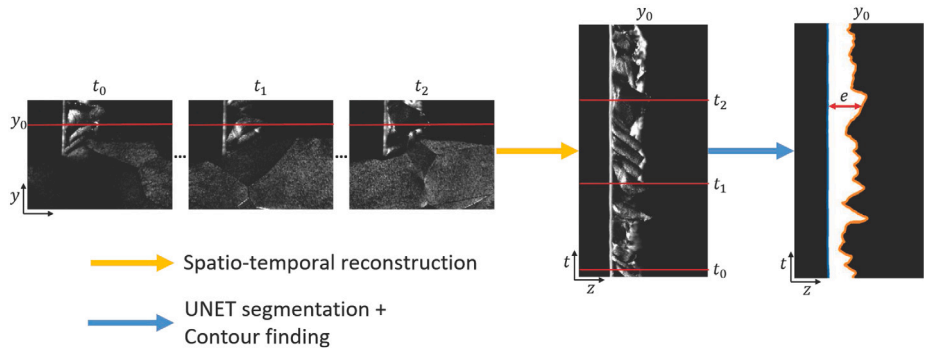

Fig. 5. Spatio-temporal reconstruction and determination of chip thickness.

work. While this network was initially developed for biomedical applications, efficient implementations have been proposed in the context of metallurgy (Perera et al., 2021) and meteorology (Cordeiro, 2020). The later version, which is referred to as the simplified U-Net algorithm, was used here. A labelled training dataset consisting of a total of 3,000 images obtained for the eight different microstructures was created from scratch. These images were manually contoured to distinguish between the tool, the specimen and the background. After training, the network provided segmented images from which the shear angle φ was evaluated. As illustrated by Fig. 4, the shear angle is defined as the angle between the line passing by the tool tip following the cutting direction and the straight line between the tool tip and the point where the chip starts to form. To evaluate the accuracy of the U-Net network, a validation dataset composed of 300 labelled images was also created. To measure the network performance, shear angle measurements were compared for manual and automated segmentation. A mean difference of 2° was observed.

2.5. Determination of chip thickness

To characterize chip morphology, a procedure based on spatio-temporal reconstruction, as introduced by Jähne (1993), was used in the present work. The underlying idea consists of reconstructing the chip resulting from a cutting test by using the corresponding set of images. As illustrated in Fig. 5, a line of pixels corresponding to a fixed vertical position y was extracted from each image. The different lines (approximately 20,000 per test per camera) were then assembled to construct a spatio-temporal image that provides temporal information regarding chip formation.

Once the reconstruction done, the U-Net algorithm (based on the simplified architecture proposed by Cordeiro (2020)) was applied to segment the spatio-temporal image and obtain the contours of the chip. Once the contours were found, the chip thickness was evaluated. The general principle of the U-Net algorithm is the same as for the determination of shear angle. The training dataset was composed of 372 images while the validation dataset consisted of 61 images. To evaluate the performance of the automated segmentation procedure, the average and standard deviation for the chip thickness were evaluated for manual and segmentation procedures. According to the results, mean errors of 7 μm and 4.5 μm were found respectively. Thanks to this procedure, the chip thickness e was obtained at each time t from the chip contours.

For the purpose of illustration, the cutting force F_z, the shear angle φ and the chip thickness e obtained for the 55 α_{wi} microstructure are plotted as a function of time t in Fig. 6. In the following, the signals obtained for the first and last 10 mm of the specimen were ignored to avoid edge effects resulting from either tool penetration or tool extraction. Also, it is important to note that, because the chosen y coordinate for the spatio-temporal reconstruction is away from the tool tip, the chip thickness e at a given time t cannot be directly compared with the corresponding force F_z and shear angle φ. Indeed, while the force and shear angle are representative of the material that is being cut at time t, the chip thickness provides some information regarding material that has already been cut. To circumvent this difficulty, the temporal analysis based on global metrics of the signal (e.g. mean value, standard deviation) is completed by an analysis in the frequency domain.

2.6. Post-processing of the different signals

Temporal analysis. The experimental data recorded during an orthogonal cutting test include different signals (e.g. force, shear angle). Any signal a consists of n data points equispaced in time with ordinates $a(t_1)$, $a(t_2)$... $a(t_n)$. To compare the signals obtained for different microstructures, it is convenient to evaluate the time-average $\bar{a}$ associated with a given test from:

$$\bar{a} = \frac{1}{n}\sum_t a(t) \tag{2}$$

Also, the standard deviation std(a) allows determining whether there are some important fluctuations of the quantity a during a test or not. For any signal a, the standard deviation std(a) is given by:

$$\mathrm{std}(a) = \sqrt{\frac{1}{n}\sum_t (a(t) - \bar{a})^2} \tag{3}$$

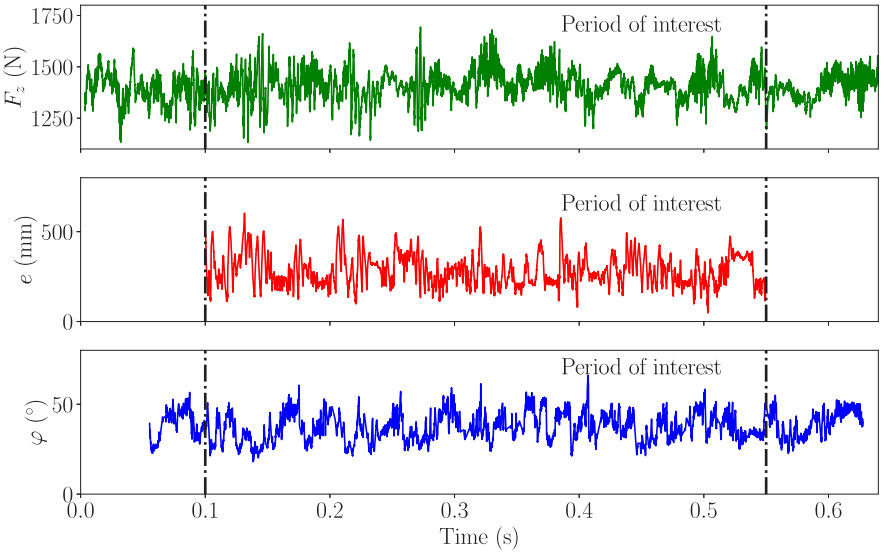

Fig. 6. Summary of temporal signals for a cutting test of $55\alpha_{wi}$ microstructure at V_c = 100 mm s^{-1}.

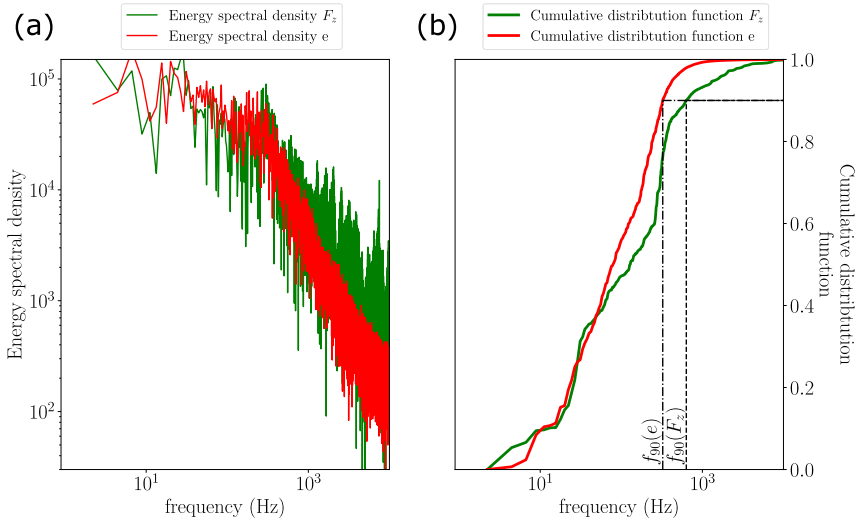

Fig. 7. Representation and comparison of (a) Energy spectral density and (b) cumulative distribution function for cutting force F_z and chip thickness e for microstructure 55 α_{wi} at V_c = 100 mm s^{-1}.

Spectral analysis. Because the signals (e.g. cutting force, chip thickness or shear angle) obtained from an orthogonal cutting test correspond to different regions of the specimen, the temporal representation is not convenient to determine whether they are similar to each other or not. Such difficulties can be circumvented with the spectral analysis of the different signals. Specifically, for any temporal signal (say a), the representation in the frequency domain (say A) is obtained using the Fast Fourier Transform (FFT) algorithm. The energy spectral density S_{aa} (Stein, 2000), that provides an estimation of the energy contained in the signal for a given frequency f, is then evaluated from the Fourier transform with:

$$S_{aa}(f) = A(f) \times A^*(f), \tag{4}$$

where A^* the complex conjugate of A.

To evaluate how the energy is distributed within the signal, it is convenient to calculate the cumulative distribution function C_a (Montgomery and Runger, 2003) associated with the energy spectral density S_{aa} from:

$$C_a(f) = \frac{\sum_{0<f'\leq f}(S_{aa}(f'))}{\sum_{0<f'\leq f_{max}}(S_{aa}(f'))} \tag{5}$$

For the purpose of illustration, the energy spectral densities obtained for the cutting force F_z and chip thickness e, as well as the corresponding cumulative distribution functions, are plotted in Fig. 7 for the $55\alpha_{wi}$ microstructure. The characteristic frequency f_{90} obtained from spectral analysis function is also provided. It corresponds to the frequency for which the cumulative distribution function reaches 90%. The characteristic frequency f_{90} thus indicates whether low or high frequencies are predominant within a signal.

To compare two temporal signals (say a and b), the Kolmogorov–Smirnov metric $D_{a,b}$ (Massey, 1951) is used to test whether they have similar frequency distributions or not. As shown in Fig. 7, the Kolmogorov–Smirnov metric $D_{a,b}$ is computed from the cumulative distribution functions C_a and C_b with:

$$D_{a,b} = \max_f \left(|C_a(f) - C_b(f)|\right) \tag{6}$$

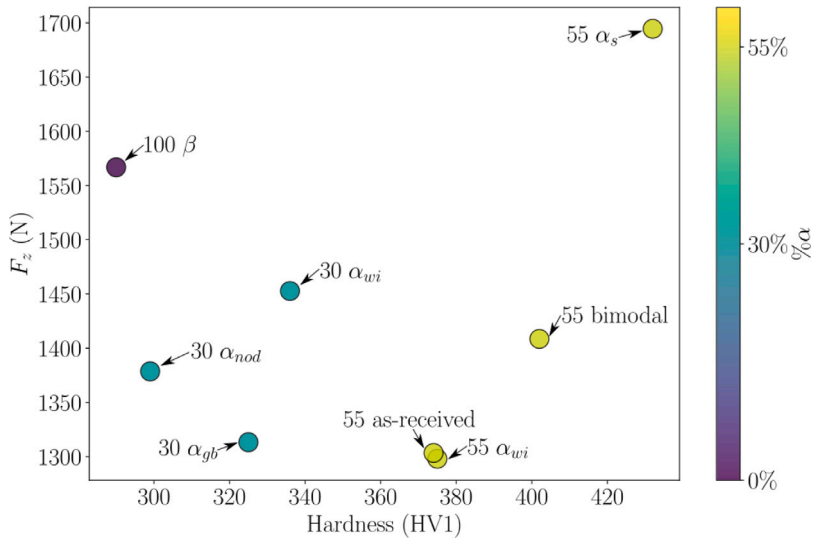

Fig. 8. Evolution of the average cutting force F_z as a function of hardness.

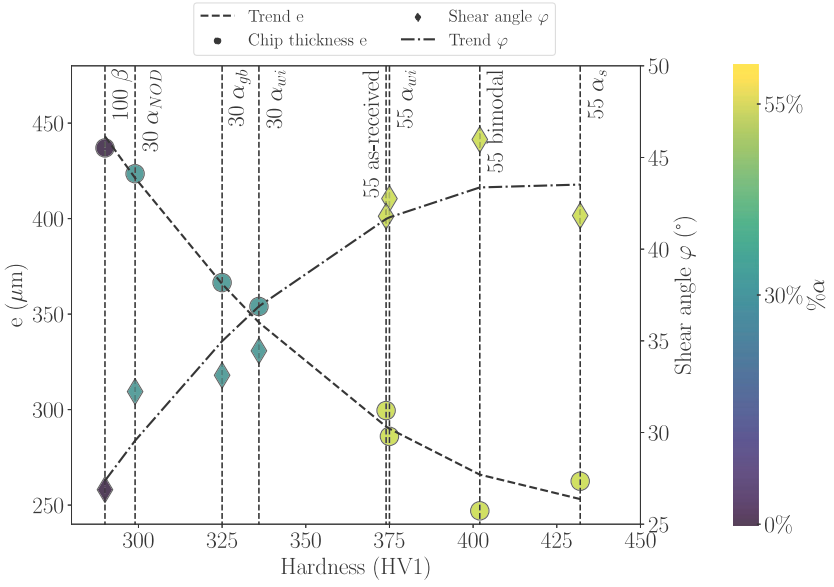

Fig. 9. Evolution of the average shear angle and chip thickness as a function of hardness.

Two frequency distributions are identical when the value of the Kolmogorov–Smirnov metric is null.

3. Results and discussion

3.1. Temporal analysis

In the present work, a minimum of two orthogonal cutting tests were performed for each microstructure. The average cutting force obtained from the mean value of the corresponding tests is plotted in Fig. 8 for the different microstructures as a function of the Vickers hardness. Though the cutting forces obtained for microstructures with similar hardness (55 α_{wi} and 55 as-received) are close, there is no obvious correlation between hardness and cutting force. Specifically, while the cutting force is maximal for the microstructure providing the highest hardness (*i.e.* 55 α_s), it remains significant for the 100 β microstructure that displays the lowest hardness. Similar conclusions have been drawn by Sharma and Meena (2020) and Abbasi et al. (2016) for the Ti6Al4V titanium alloy while (Suárez Fernández et al., 2021) observed an increasing machining force with decreasing hardness for the Ti6246 alloy. Also, it is worth noticing that there is no obvious connection between the average cutting force and the α phase fraction. For instance, both the minimal and maximal cutting forces are obtained for a phase fraction of 55%.

The average chip thickness and shear angles that characterize chip morphology are plotted as a function of hardness in Fig. 9. According to the results, the chip thickness decreases with an increasing hardness while the opposite trend is observed for the shear angle. These results indicate that, for microstructures that result in low hardness, the plastic deformation process leading to chip formation starts far away from the tool tip, which increases the chip thickness. As a consequence, for a given α-phase fraction, the presence of fine α particles (e.g. 55 α_s microstructure) that tend to increase hardness leads to a reduction of the average chip thickness. Also, such results suggest that the cutting force is governed by the competition between two aspects. On the one hand, the flow stress of hard materials is important; such materials

Table 2
Kolmogorov–Smirnov coefficient $D_{F_z,e}$ obtained when comparing frequency responses of chip thickness e and cutting force F_z.

		0% α	30% α			55% α			
		F_z 100% β	F_z 33% α_{gb+wgb}	F_z 34% α_{wi}	F_z 30% α_{NOD}	F_z 55% α_{wi}	F_z 55% α_s	F_z 48% α_s+ 12% α_{NOD}	F_z 34% α_s+ 21% α_{NOD}
0% α	e 100% β	0.09	0.26	0.29	0.38	0.46	0.45	0.63	0.58
30% α	e 33% α_{gb+wgb}	0.22	0.04	0.07	0.16	0.30	0.31	0.44	0.38
	e 34% α_{wi}	0.26	0.08	0.11	0.18	0.32	0.32	0.48	0.41
	e 30% α_{NOD}	0.33	0.13	0.11	0.08	0.31	0.32	0.45	0.39
55% α	e 55% α_{wi}	0.47	0.38	0.38	0.35	0.13	0.10	0.14	0.17
	e 55% α_s	0.43	0.35	0.35	0.33	0.23	0.20	0.20	0.25
	e 48% α_s + 12% α_{NOD}	0.64	0.51	0.53	0.48	0.25	0.27	0.10	0.20
	e 34% α_s + 21% α_{NOD}	0.50	0.36	0.37	0.33	0.10	0.13	0.15	0.08

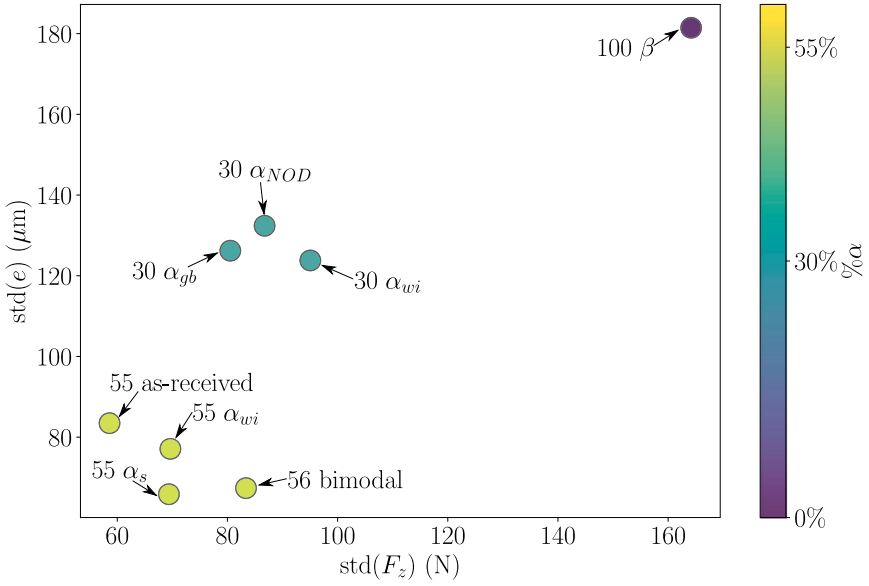

Fig. 10. Representation of the standard deviation for chip thickness e and cutting force F_z for each microstructure.

thus demand important cutting forces. On the other hand, the amount of material being deformed at a given time is generally higher for microstructures providing low hardness, which causes the cutting force to increase. In order to reduce cutting forces, the hardness of the optimal microstructure is therefore intermediate. It corresponds to a compromise between the resistance to plastic deformation and the size of the zone where plastic deformation is significant.

The standard deviations associated with the chip thickness std(e) and the cutting force std(F_z) are plotted in Fig. 10. For a given microstructure, these quantities allow evaluating whether there are some important fluctuations of the thickness and the cutting force or not. According to the results, the standard deviations for the cutting force and chip thickness are strongly correlated with each other. The 100 β microstructure displays the highest standard deviations. At the opposite, standard deviations are largely reduced for the microstructure with α particles resulting from secondary precipitation (55 α_s). It is possible to distinguish three different clusters as a function of the α phase volume fraction. The fluctuations observed for the cutting force and chip thickness are therefore primarily impacted by the α phase volume fraction. Other microstructural features (e.g. morphology, size of α particles) have little influence.

3.2. Spectral analysis

The spectral analysis allows evaluating the discrepancies between force and chip thickness signals. The corresponding Kolmogorov–Smirnov metric $D_{F_z,e}$ is presented in the form of a matrix (see Table 2) that indicates whether the force signal obtained for a given microstructure is similar to the chip thickness signal of another microstructure. Generally speaking, the diagonal values of the Kolmogorov–Smirnov metric $D_{F_z,e}$ are the lowest. For a given microstructure, the force and thickness signals are therefore very similar, hence correlated to each other. Such results suggest that the mechanical response of a given microstructure is conditioned by chip morphology. This observation is echoing the results of Joshi et al. (2014) who found close frequencies when comparing chip segmentation to cutting forces. Also, the Kolmogorov–Smirnov metric $D_{F_z,e}$ calculated for two different microstructures is low, provided that these microstructures have similar fractions of α phase. At the opposite, for microstructures with different fractions of α phase, important discrepancies exist between the cutting force and chip thickness signals. Such results confirm that the response of a given microstructure is primarily controlled by the α phase volume fraction.

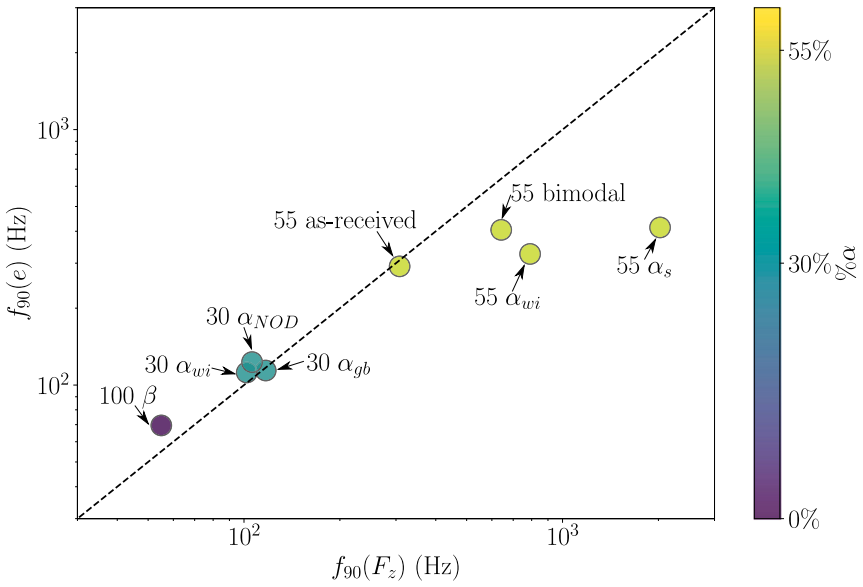

Fig. 11. Characteristic frequencies obtained for cutting force and chip thickness signals for the different microstructures.

The characteristic frequencies f_{90} calculated for the cutting force and chip thickness are plotted in Fig. 11. According to the results, the characteristic frequencies span over different orders of magnitude. The clusters corresponding to different fractions of α phase are also visible in this representation. The lowest characteristic frequency is obtained for the 100 β microstructure, for which no fine microstructural details exist. At the opposite, the 55 α_s microstructure, which contains the finest dispersion of α precipitates, displays the highest characteristic frequency. Though the cutting force and chip thickness are obtained from independent measurements, their characteristic frequencies are close. However, microstructures with a α phase fraction of 55% do not exactly follow this trend. For these microstructures, the characteristic frequency of the force signal is superior to that of the chip thickness signal. At this stage, the reason for such differences is not identified.

A graphical comparison can also be conducted thanks to the spatio-temporal reconstruction. Indeed, as illustrated by Fig. 12, the impact of microstructure on chip morphology can be observed from the spatio-temporal reconstruction of chips. Specifically, the reduction of chip thickness caused by the increase of α phase volume fraction is clearly visible. Fig. 12 also illustrates that the segmentation frequency increases with the α phase volume fraction. Indeed, the time interval between two consecutive segments is reduced when the fraction of α phase is increased. These results indicate that the α phase promote strain localization, hence chip segmentation. Such observations are consistent with the experimental observations of Boubaker et al. (2019) who found that, because of a lower strain-rate sensitivity, $\alpha + \beta$ microstructures are more prone to shear banding than β microstructures.

4. Conclusions

In this work, the impact of microstructure on chip formation and cutting force during orthogonal cutting tests of the Ti5553 alloy has been investigated. For this purpose, seven microstructures with different fractions, sizes and morphologies of α-phase particles were generated from the as-received microstructure. A specific experimental set-up including two high-speed cameras and a dynamometer was developed. A novel post-processing procedure that relies on machine learning provided the temporal evolutions of the shear angle and the chip thickness. Also, spectral analysis was extensively used to evaluate whether two signals (e.g. force and thickness) are similar or not. The results of the present study indicate that:

1. No direct link can be established between the cutting force and the hardness. The highest cutting forces are recorded for microstructures providing either high or low hardness. On the one hand, the deformed volume is important for microstructures that display low hardness, which causes the cutting force to increase. On the other hand, hard materials with high yield stresses also require an important cutting force.
2. The variations of the cutting force and chip thickness during a single test depends on microstructure. Such variations are primarily affected by the fraction of α phase (0%, 30% or 55%). The size and morphology of α particles have no visible influence.
3. For a given microstructure, the frequency distributions of the force and chip thickness signals are very similar. Both quantities are correlated to each other.
4. The frequency distributions for the force and chip thickness signals are shifted towards high frequencies when the fraction of α phase increases.
5. Chip morphology is affected by the microstructure. It is noteworthy that the mean chip thickness is reduced when the α phase volume fraction is larger. Moreover, the segmentation is also impacted by microstructure. Indeed for microstructures with a small amount of α phase only a few large segments are observed while a high fraction of α phase leads to small segments that appear more frequently.

The results presented in this study indicate that microstructure optimization provides a way of reducing cutting forces when machining the Ti5553 titanium alloy. Specifically, microstructures with an intermediate hardness generate low cutting forces, which is expected to reduce tool wear, and hence improve productivity. Future work should focus on the impact of the cutting speed on chip formation. The same experimental set-up and post-processing procedures will be used to evaluate the sensitivity of the different microstructures to the cutting speed. Also, the experimental results obtained in the present study provide valuable data for comparison with numerical results. The experimental dataset will be used to determine whether the microstructure-sensitive constitutive models used in the context of machining (Boubaker, 2019) are relevant or not.

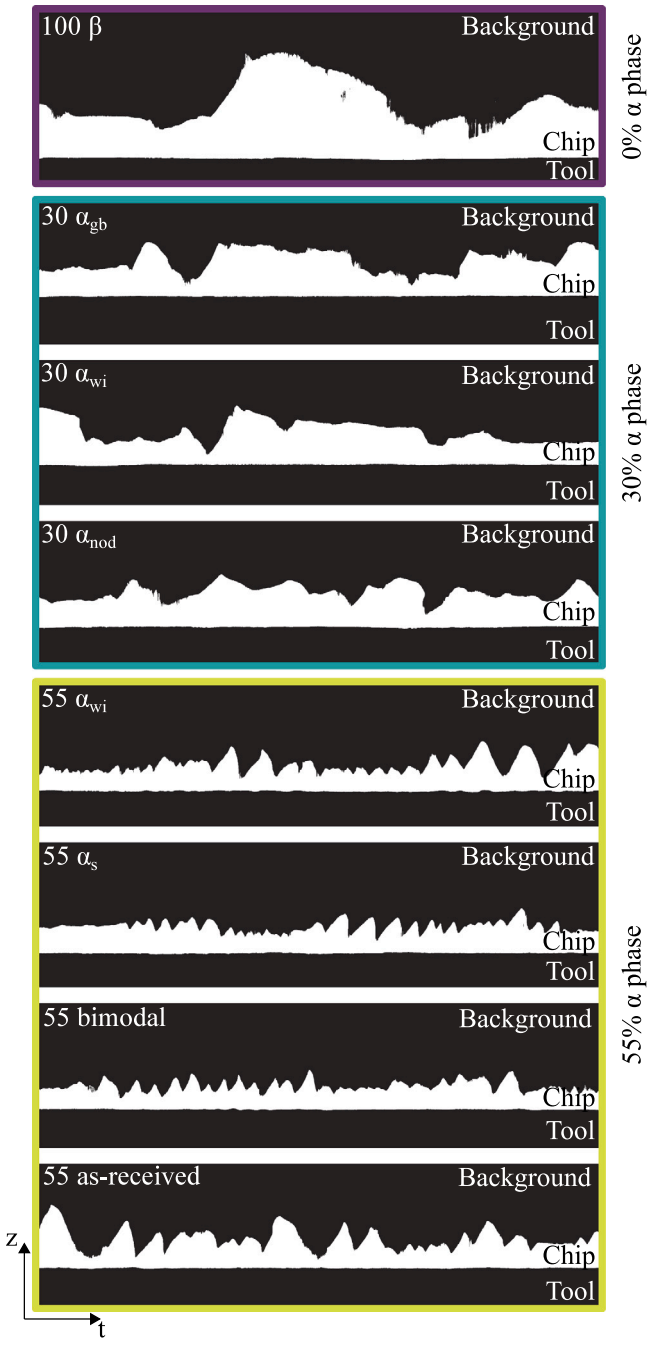

Fig. 12. Representation of different spatio-temporal reconstructions for each microstructure.

CRediT authorship contribution statement

A. Pouliquen: Conceptualization, Methodology, Software, Investigation, Writing – original draft, Visualization, Formal analysis. **N. Chanfreau:** Methodology, Formal analysis, Investigation. **L. Gallegos-Mayorga:** Methodology, Validation, Investigation, Writing – review & editing. **C. Mareau:** Methodology, Validation, Writing – review & editing. **Y. Ayed:** Methodology, Validation, Writing – review & editing. **G. Germain:** Methodology, Validation, Resources, Writing – review & editing, Supervision, Funding acquisition. **M. Dehmas:** Writing – review & editing, Supervision, Project administration, Funding acquisition.

Declaration of competing interest

The authors declare the following financial interests/personal relationships which may be considered as potential competing interests: Guenael Germain reports equipment, drugs, or supplies was provided by Timet. Gueneal Germain reports equipment, drugs, or supplies was provided by Seco Tools AB. Antoine Pouliquen reports writng assistance was provided by CIRIMAT.

Data availability

The authors do not have permission to share data

Acknowledgements

The authors gratefully acknowledge the French National Research Agency (ANR) under the framework of the DEMUTI project for the financial support and also TIMET Savoie and SECO Tools AB for their technical and material support. The authors are grateful to everyone who contributed to this research, including Quentin Hatte and the HPC Cassiopée team who helped to implement the various experiments and analyses.

References

Abbasi, S.A., Feng, P., Ma, Y., Zhang, J., Yu, D., Wu, Z., 2016. Influence of microstructure and hardness on machinability of heat-treated titanium alloy Ti-6Al-4V in end milling with polycrystalline diamond tools. Int. J. Adv. Manuf. Technol. 86 (5–8), 1393–1405. http://dx.doi.org/10.1007/s00170-015-8245-1.

Arrazola, P.J., Garay, A., Iriarte, L.M., Armendia, M., Marya, S., Le Maître, F., 2009. Machinability of titanium alloys (Ti6Al4V and Ti555.3). J. Mater Process. Technol. 209 (5), 2223–2230. http://dx.doi.org/10.1016/j.jmatprotec.2008.06.020.

Attanasio, A., Gelfi, M., Pola, A., Ceretti, E., Giardini, C., 2013. Influence of material microstructures in micromilling of Ti6Al4V alloy. Materials 6 (9), 4268–4283. http://dx.doi.org/10.3390/ma6094268.

Ayed, Y., Germain, G., 2018. High-pressure water-jet-assisted machining of Ti555-3 titanium alloy: investigation of tool wear mechanisms. Int. J. Adv. Manuf. Technol. 96 (1), 845–856. http://dx.doi.org/10.1007/s00170-018-1661-2.

Ayed, Y., Germain, G., Melsio, A.P., Kowalewski, P., Locufier, D., 2017. Impact of supply conditions of liquid nitrogen on tool wear and surface integrity when machining the Ti-6Al-4V titanium alloy. Int. J. Adv. Manuf. Technol. 93 (1), 1199–1206. http://dx.doi.org/10.1007/s00170-017-0604-7.

Baizeau, T., Campocasso, S., Fromentin, G., Besnard, R., 2017. Kinematic field measurements during orthogonal cutting tests via dic with double-frame camera and pulsed laser lighting. Exp. Mech. 57 (4), 581–591. http://dx.doi.org/10.1007/s11340-016-0248-9.

Barry, J., Byrne, G., Lennon, D., 2001. Observations on chip formation and acoustic emission in machining Ti–6Al–4V alloy. Int. J. Mach. Tools Manuf. 41 (7), 1055–1070. http://dx.doi.org/10.1016/S0890-6955(00)00096-1.

Boubaker, H.B., 2019. Développement d'une modélisation à l'échelle cristalline d'un alliage de titane pour la simulation de l'usinage (Ph.D. thesis). Université d'Angers.

Boubaker, H., Mareau, C., Ayed, Y., Germain, G., Tidu, A., 2019. Impact of the initial microstructure and the loading conditions on the deformation behavior of the Ti17 titanium alloy. J. Mater. Sci. 55, 1765–1778. http://dx.doi.org/10.1007/s10853-019-04014-5.

Bouchnak, T.B., 2010. Etude du comportement en sollicitations extrêmes et de l'usinabilite d'un nouvel alliage de titane aeronautique : le Ti555-3 (Ph.D. thesis). Arts et Métiers ParisTech.

Cordeiro, M., 2020. Creating a very simple u-net model with pytorch for semantic segmentation of satellite images. https://medium.com/analytics-vidhya/creating-a-very-simple-u-net-model-with-pytorch-for-semantic-segmentation-of-satellite-images-223aa216e705.

Harzallah, M., Pottier, T., Gilblas, R., Landon, Y., Mousseigne, M., Senatore, J., 2018. A coupled in-situ measurement of temperature and kinematic fields in Ti-6Al-4V serrated chip formation at micro-scale. Int. J. Mach. Tools Manuf. 130–131, 20–35. http://dx.doi.org/10.1016/j.ijmachtools.2018.03.003.

Hijazi, A., Madhavan, V., 2008. A novel ultra-high speed camera for digital image processing zpplications. Meas. Sci. Technol. 19 (8), 085503. http://dx.doi.org/10.1088/0957-0233/19/8/085503.

Jähne, B., 1993. Motion in space-time images. In: Spatio-Temporal Image Processing: Theory and Scientific Applications. In: Lecture Notes in Computer Science, Springer, Berlin, Heidelberg, pp. 76–109. http://dx.doi.org/10.1007/3-540-57418-2_16.

Joshi, S., Pawar, P., Tewari, A., Joshi, S.S., 2014. Effect of β phase fraction in titanium alloys on chip segmentation in their orthogonal machining. CIRP J. Manuf. Sci. Technol. 7 (3), 191–201. http://dx.doi.org/10.1016/j.cirpj.2014.03.001.

Kaynak, Y., Gharibi, A., Ozkutuk, M., 2018. Experimental and numerical study of chip formation in orthogonal cutting of Ti-5553 alloy: the influence of cryogenic, MQL, and high pressure coolant supply. Int. J. Adv. Manuf. Technol. 94 (1), 1411–1428. http://dx.doi.org/10.1007/s00170-017-0904-y.

Kieren-Ehses, S., Böhme, L., Morales-Rivas, L., Lösch, J., Kirsch, B., Kerscher, E., Kopnarski, M., Aurich, J.C., 2021. The influence of the crystallographic orientation when micro machining commercially pure titanium: A size effect. Precis. Eng. 72, 158–171. http://dx.doi.org/10.1016/j.precisioneng.2021.04.007.

Liu, Y., Zhang, D., Geng, D., Shao, Z., Zhou, Z., Sun, Z., Jiang, Y., Jiang, X., 2022. Ironing effect on surface integrity and fatigue behavior during ultrasonic peening drilling of Ti-6Al-4V. Chin. J. Aeronaut. http://dx.doi.org/10.1016/j.cja.2022.12.009, URL https://www.sciencedirect.com/science/article/pii/S1000936122003028.

Massey, F.J., 1951. The Kolmogorov-Smirnov test for goodness of fit. J. Amer. Statist. Assoc. 46 (253), 68–78. http://dx.doi.org/10.2307/2280095.

Mo, S., Axinte, D., Hyde, T., Gindy, N., 2005. An example of selection of the cutting conditions in broaching of heat-resistant alloys based on cutting forces, surface roughness and tool wear. J. Mater Process. Technol. 160 (3), 382–389. http://dx.doi.org/10.1016/j.jmatprotec.2004.06.026, URL https://linkinghub.elsevier.com/retrieve/pii/S0924013604008763.

Montgomery, C., Runger, G., 2003. Discrete random variables and probability distributions. In: Applied Statistics and Probability for Engineers. John Wiley & Sons, pp. 59–97.

Moulart, R., Fouilland, L., El Mansori, M., 2019. Développement d'une méthode de mesure de champs cinématiques pour étudier la coupe à chaud. https://hal.archives-ouvertes.fr/hal-01178165/document.

Niknam, S.A., Khettabi, R., Songmene, V., 2014. Machinability and machining of titanium alloys: A review. In: Davim, J.P. (Ed.), Machining of Titanium Alloys. Springer Berlin Heidelberg, Berlin, Heidelberg, pp. 1–30. http://dx.doi.org/10.1007/978-3-662-43902-9_1.

Nouari, M., Calamaz, M., Girot, F., 2008. Mécanismes d'usure des outils coupants en usinage à Sec de l'alliage de Titane Aéronautique Ti–6Al–4V. C. R. Méc. 336 (10), 772–781. http://dx.doi.org/10.1016/j.crme.2008.07.007.

Patil, S., Kekade, S., Phapale, K., Jadhav, S., Powar, A., Supare, A., Singh, R., 2016. Effect of α and β phase volume fraction on machining characteristics of titanium alloy Ti6Al4V. 16th Machining Innovations Conference for Aerospace Industry - MIC 2016, Procedia Manuf. 16th Machining Innovations Conference for Aerospace Industry - MIC 2016, 6, 63–70.http://dx.doi.org/10.1016/j.promfg.2016.11.009,

Perera, R., Guzzetti, D., Agrawal, V., 2021. Optimized and autonomous machine learning framework for characterizing pores, particles, grains and grain boundaries in microstructural images. Comput. Mater. Sci. 196, 110524. http://dx.doi.org/10.1016/j.commatsci.2021.110524.

Pottier, T., Germain, G., Calamaz, M., Morel, A., Coupard, D., 2014. Sub-millimeter measurement of finite strains at cutting tool tip vicinity. Exp. Mech. 54 (6), 1031–1042. http://dx.doi.org/10.1007/s11340-014-9868-0.

Ramirez, C., 2017. Optimization criteria of titanium alloys to improve their machinability (Ph.D. thesis). (2017ENAM0006), Ecole Nationale d'arts et métiers, ENSAM.

Rech, J., Yen, Y.-C., Hamdi, H., Altan, T., Bouzakis, K.D., 2004. Influence of cutting edge radius of coated tool in orthogonal cutting of alloy steel. AIP Conf. Proc. 712 (1), 1402–1407. http://dx.doi.org/10.1063/1.1766725, URL http://aip.scitation.org/doi/10.1063/1.1766725, Publisher: American Institute of Physics.

Ronneberger, O., Fischer, P., Brox, T., 2015. U-net: convolutional networks for biomedical image segmentation. In: Medical Image Computing and Computer-Assisted Intervention. MICCAI, In: LNCS, vol. 9351, Springer, pp. 234–241, URL http://lmb.informatik.uni-freiburg.de/Publications/2015/RFB15a, (available on arXiv:1505.04597 [cs.CV]).

Sharma, S., Meena, A., 2020. Microstructure attributes and tool wear mechanisms during high-speed machining of Ti-6Al-4V. J. Manuf. Process. 50, 345–365. http://dx.doi.org/10.1016/j.jmapro.2019.12.029.

Stein, J., 2000. The frequency domain. In: Digital Signal Processing: A Computer Science Perspective, Wiley John Wiley & Sons, pp. 103–161.

Suárez Fernández, D., Wynne, B.P., Crawforth, P., Jackson, M., 2021. Titanium alloy microstructure fingerprint plots from in-process machining. Mater. Sci. Eng. A 811, 141074. http://dx.doi.org/10.1016/j.msea.2021.141074.

Sun, S., Brandt, M., Dargusch, M., 2009. Characteristics of cutting forces and chip formation in machining of titanium alloys. Int. J. Mach. Tools Manuf. 49, 561–568. http://dx.doi.org/10.1016/j.ijmachtools.2009.02.008, URL https://www.sciencedirect.com/science/article/abs/pii/S0890695509000558?via%3Dihub#preview-section-cited-by.

Voort, G.F.V., 1999. Metallography, Principles and Practice, ASM International.

Wagner, V., Barelli, F., Dessein, G., Laheurte, R., Darnis, P., Cahuc, O., Mousseigne, M., 2019. Comparison of the chip formations during turning of Ti64 β and Ti64 $\alpha+\beta$. Proc. Inst. Mech. Eng. B 233 (2), 494–504. http://dx.doi.org/10.1177/0954405417728309, URL http://journals.sagepub.com/doi/10.1177/0954405417728309.

Zhang, D., Meurer, M., Zhang, X., Bergs, T., Ding, H., 2021. Understanding kinematics of the orthogonal cutting using digital image correlation measurement and analysis. J. Manuf. Sci. Eng. 144 (3), http://dx.doi.org/10.1115/1.4051917.